

Modeling light vs. current characteristics of long-wavelength VCSELs with various DBR materials

J. Piprek

University of Delaware, Materials Science Program
Newark, DE 19716-3106, USA

H. Wenzel

Ferdinand-Braun-Institut für Höchstfrequenztechnik
Rudower Chaussee 5-7, 12489 Berlin, Germany

H.-J. Wünsche, D. Braun, and F. Henneberger

Humboldt-Universität, Institut für Physik, Photonik
Invalidenstr. 110, 10115 Berlin, Germany

ABSTRACT

Long-wavelength vertical-cavity surface-emitting lasers (LW-VCSELs) are investigated using electro-thermal, optical, and electronic modeling. The strain-compensated InGaAsP multi-quantum-well active region of the device example is vertically sandwiched between various distributed Bragg reflectors (DBRs). InP/InGaAsP, Si/SiO₂, and GaAs/AlAs mirrors are considered as well as novel combinations like SiC/MgO. The model includes nonuniform current injection, distributed heat sources, temperature dependent material properties, and **k-p** band structure calculations. Device parameters such as thermal resistance, threshold current, and external quantum efficiency are compared and heating effects are evaluated. Simulated light power vs. current characteristics exhibit the typical thermal roll-over in continuous wave operation. The complex influence of the DBR materials is analyzed in detail.

Keywords: vertical-cavity surface-emitting laser diode, distributed Bragg reflector, laser modeling

1 INTRODUCTION

Long-wavelength (1.3–1.6 μm) vertical-cavity surface-emitting lasers are a promising new generation of light sources for long-distance optical communication systems. Compared to their edge-emitting counterparts, LW-VCSELs are expected to exhibit advantages in testing, optical coupling, single-mode operation, and modulation. InGaAsP/InP LW-VCSELs have been proposed first, when the detailed concept of surface-emitting laser diodes was introduced.¹ But near room temperature (14 °C) continuous wave (CW) operation of an electrically pumped

1.3 μm device has been achieved only recently,² despite the rapid development of AlGaAs VCSELs emitting in the 0.8–1.0 μm wavelength range. This contrast is mainly attributed to the InGaAsP material system with larger Auger nonradiative recombination, higher intervalence band absorption, lower thermal conductivity, and smaller refractive index variation than in the AlGaAs system.

Different concepts of LW-VCSELs are currently competing, featuring alternative materials of the distributed Bragg reflectors or strained multi-quantum-well (MQW) active regions. The substrate (bottom) site mirror materials are InP/InGaAsP,^{3,4} GaAs/AlAs,^{5,6} or dielectric materials, e.g., Si/SiO₂.^{2,7} The top DBR is commonly a Si/SiO₂,^{7,5} Si/Al₂O₃³ or Si/SiN_x⁸ dielectric mirror (Si denotes amorphous material), whereas a Si/MgO DBR with higher thermal conductivity was utilized to achieve the 14°C CW performance in top-down mounting.² Recent concepts also include a GaAs/AlAs top mirror.^{4,6} Most of these devices employ bulk InGaAsP as active region, but some of them also include unstrained⁷ or strain-compensated^{9,6} MQW active regions.

Computer modeling and simulation is often used to analyze and to optimize VCSELs. In the case of AlGaAs VCSELs, numerical models of thermal, optical, and electronic processes have been combined to calculate light power vs. current (*PI*) characteristics.^{10–12} A time-dependent numerical model of VCSELs is described in Ref.¹³ For LW-VCSELs, models of thermal,^{14–17} optical¹⁹ or electronic^{8,9} properties have been applied separately. This paper presents the first *PI* simulation of InGaAsP LW-VCSELs combining electro-thermal, optical, and gain function calculations. The electro-thermal simulation employs quasi three-dimensional (3D) finite element analysis and calculates the cylinder symmetrical temperature distribution $T(r, z)$, considering nonuniform heat source distributions (Section 3). Transfer matrix optical modeling gives the threshold optical field along the laser axis and leads to threshold gain g_{th} , emission wavelength λ_o and external quantum efficiency η (Section 4). The gain vs. carrier density function is obtained from **k**·**p** band structure calculations for strained quantum wells and leads to the threshold current I_{th} (Section 5). Finally, simulated *PI* characteristics are used to investigate the influence of DBR materials on laser operation (Section 6). Material parameters are mostly taken from Refs.^{20–23}

2 DEVICE CONSIDERATIONS

The center part of the example device is displayed in Fig. 1. The intended emission wavelength is $\lambda_o=1.55 \mu\text{m}$. Our strain-compensated InGaAsP MQW consists of 13 quantum wells with 1% compressive strain and 14 barriers with 1% tensile strain, each 4 nm thick. The undoped active region is sandwiched between 918 nm p-doped InP top spacer and 552 nm n-doped InP bottom spacer (10^{18} cm^{-3} doping density) to form a total optical spacer thickness of $3.75 \cdot \lambda_o$. Semi-insulating InP is used as regrowth material. Different combinations of top and bottom mirror materials are attached ($\lambda/4$ sheet thicknesses), starting with the lower and the higher refractive index material, respectively ($2 \cdot 10^{18} \text{ cm}^{-3}$ doping of semiconductor mirrors). The Au p-contact is 270 nm thick, the diameters of top window, active region, and top DBR are 6 μm , 10 μm , and 15 μm , respectively. Substrate thickness and device radius are 100 μm .

Tab. 1 lists known physical parameters of various material combinations to form multilayer mirrors. Most critical are the refractive index step and the thermal conductivity. InP/InGaAsP mirrors require almost double the number of layers than GaAs/AlAs mirrors to reach the same reflectivity. This is connected with a strong increase in the thermal resistance of the bottom mirror. Dielectric bottom mirrors, e.g., Si/SiO₂ within a hole etched into the substrate need only a few layers, but the thermal resistance in top-down mounting is high, too.¹⁶ Material choices for dielectric top DBRs mostly include amorphous Silicon with high refractive index but low thermal conductivity and high optical absorption. Thus, SiC was proposed¹⁷ to replace Si. Lowest laser heating is expected with SiC/BeO mirrors since both amorphous materials have the highest thermal conductivity in Tab. 1. But BeO is very difficult to handle in the technological process and it is not considered further. Finally, Si/Al₂O₃ and Si/SiN_x top DBRs as well as the novel combinations TiO₂/SiO₂²² and ZnSe/CaF₂¹⁸ show no overall advantage and they are also excluded from the following comparison.

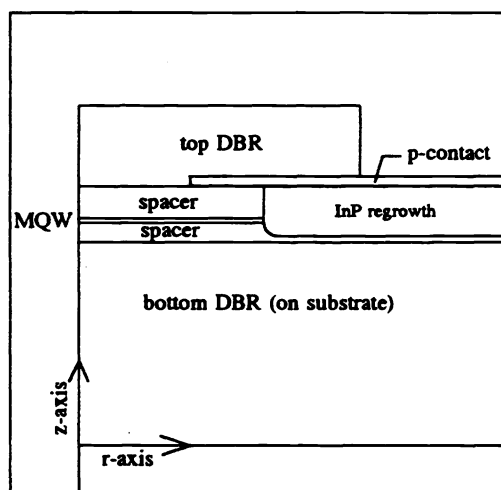


Figure 1: Diagram of the top central LW-VCSEL section in cylinder coordinates (r, z) as assumed in the calculations (top-mounted case).

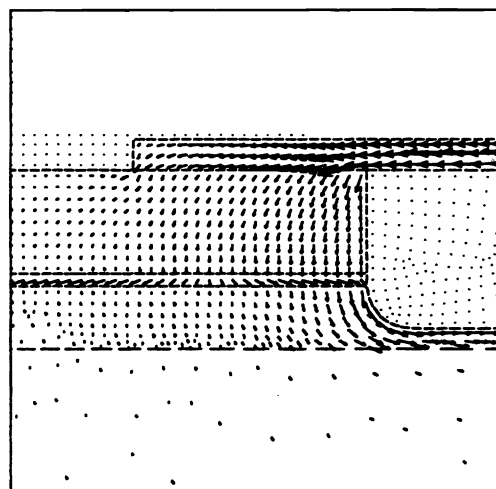


Figure 2: Vectorial display of the current density distribution $\vec{j}(r, z)$ near the p-contact as calculated from (6) (one vector per element, vector length gives j).

DBR Materials	E_g [eV]	n	dn/dT [K^{-1}]	α [cm^{-1}]	κ [$Wcm^{-1}K^{-1}$]
InP	1.34	3.17	$3 \cdot 10^{-4}$	2	0.68
InGaAsP ($1.44\mu m$)	0.86	3.46	$7 \cdot 10^{-4}$	2	0.042
GaAs	1.42	3.38	$4 \cdot 10^{-4}$	6	0.44
AlAs	2.22	2.91	$1 \cdot 10^{-4}$	6	0.91
Si	1.4	3.3	$1 \cdot 10^{-4}$	800	0.026
SiO ₂	9.0	1.44	$1 \cdot 10^{-5}$		0.014
Si	1.4	3.3	$1 \cdot 10^{-4}$	800	0.026
Si ₃ N ₄	3.9	1.90			0.16
Si	1.4	3.3	$1 \cdot 10^{-4}$	800	0.026
Al ₂ O ₃	7.3	1.74			0.36
TiO ₂	3.0	2.44		20	0.089
SiO ₂	9.0	1.44	$1 \cdot 10^{-5}$		0.014
ZnSe	2.7	2.46	$2 \cdot 10^{-4}$		0.19
CaF ₂	11.2	1.43	$-1 \cdot 10^{-5}$		0.1
Si	1.4	3.3	$1 \cdot 10^{-4}$	800	0.026
MgO	5.4	1.71	$1 \cdot 10^{-5}$		0.53
SiC	2.6	2.57	$7 \cdot 10^{-5}$		2.5
MgO	5.4	1.71	$1 \cdot 10^{-5}$		0.53
SiC	2.6	2.57	$7 \cdot 10^{-5}$		2.5
BeO	10.6	1.68	$1 \cdot 10^{-5}$		2.3

Table 1: Properties of DBR materials at room temperature: E_g – energy band gap, n – refractive index at $1.55\mu m$ wavelength (0.8 eV), α – absorption coefficient ($\lambda=1.55 \mu m$, electron density $2 \cdot 10^{18} cm^{-3}$), κ – thermal conductivity.

3 HEAT SOURCES AND TEMPERATURE

Laser heating is responsible for the typical *PI* roll-over of VCSELs at higher currents and, until today, it prevents CW operation of LW-VCSELs at room temperature. Thus, thorough thermal modeling is essential for *PI* simulation. The cylinder symmetrical temperature distribution $T(r, z)$ within the VCSEL is obtained by solving the stationary thermal conduction equation

$$\frac{\partial}{\partial r} \kappa_r \frac{\partial T}{\partial r} + \frac{1}{r} \kappa_r \frac{\partial T}{\partial r} + \frac{\partial}{\partial z} \kappa_z \frac{\partial T}{\partial z} = -w(r, z), \quad (1)$$

with the boundary conditions $T=300$ K at the heat sink and zero heat flux through all other laser surfaces. The parameter $\kappa(r, z)$ gives the thermal conductivity in vertical (κ_z) or in radial (κ_r) direction. Anisotropic behavior ($\kappa_z \neq \kappa_r$) occurs in multi-layer materials like DBRs. Employing the simple model of serial and parallel thermal resistances, resp., the two components of the DBR thermal conductivity are calculated as

$$\kappa_r = (d_1 \kappa_1 + d_2 \kappa_2) / (d_1 + d_2) \quad \text{and} \quad \kappa_z = (d_1 + d_2) / (d_1 / \kappa_1 + d_2 / \kappa_2) \quad (2)$$

(layer thicknesses d_1, d_2 and bulk thermal conductivities κ_1, κ_2). In the case of dielectric top-DBRs, each layer is described by its bulk thermal conductivity. The parameter κ also depends on the temperature, following approximately $T^{-1.375}$ for InGaAsP and AlGaAs. The heat power density $w(r, z)$ in (1) includes different heat sources with different spatial distributions. Joule heating

$$w_j(r, z) = \rho(r, z) j^2(r, z) \quad (3)$$

depends on the current density j and the (anisotropic) electrical resistivity ρ . In our bulk semiconductor materials, Joule heating is relatively small. Only at the p-contact and within the semiconductor DBRs, severe heating can be produced by interface resistances. For the p-contact, a resistance of $R_{con}=50 \Omega$ is assumed. The conduction band offset within our semiconductor mirrors is less than 0.2 eV and heat is mainly generated in p-doped DBRs.¹² Since the electrical current only flows through the n-doped bottom DBR in our device, mirror heating is neglected. Another kind of heat source is caused by reabsorption of radiation. The spontaneous radiation which leaves the MQW active region is absorbed in the entire device and has no remarkable influence on the cavity heating. Regarding stimulated radiation above laser threshold, the part $(1 - \eta)$ of the total light power is absorbed within the optical cavity according to the absorption coefficients α of the different layers (see Tabs. 1 and 3). For most of the amorphous mirror materials, no applicable absorption data have been found. Thus, absorption within the DBR is excluded from our comparison. The absorbed light power is assumed to be homogeneously distributed within the active region

$$w_{abs} = U_a(1 - \eta)(I - I_{th}) / d_a A_a \quad (4)$$

with d_a, A_a, U_a, I , and I_{th} giving total thickness of the quantum wells, area and voltage of the active region, total current, and threshold current, respectively. Within the MQW active region, heat is also generated by nonradiative recombination

$$w_{nr}(r) = e U_a R_{nr}(r) \quad (5)$$

with elementary charge e and recombination rate R_{nr} , determined from the carrier distribution $N(r)$ (see below).

In general, the semiconductor transport equations¹³ have to be solved to obtain the current density and the quantum well recombination rate as function of the carrier density of electrons and holes. In this paper, the heat density distributions (3) and (5) are calculated using a simplified approach. Outside the MQW, drift is expected to dominate the electron flow in the n-doped region as well as the hole flow in the p-doped region. Current density vector \vec{j} (see Fig. 2) and Joule heat w_j are calculated here from the electrostatic potential $U(r, z)$ solving

$$\frac{\partial}{\partial r} \rho^{-1} \frac{\partial U}{\partial r} + \frac{1}{r} \rho^{-1} \frac{\partial U}{\partial r} + \frac{\partial}{\partial z} \rho^{-1} \frac{\partial U}{\partial z} = 0 \quad (6)$$

with constant potential at the contacts and zero flux through all other surfaces. The resulting hole injection current into the active region $j_a(r)$ is maximum at the perimeter (see Fig. 5). Inside the active layers, the radial

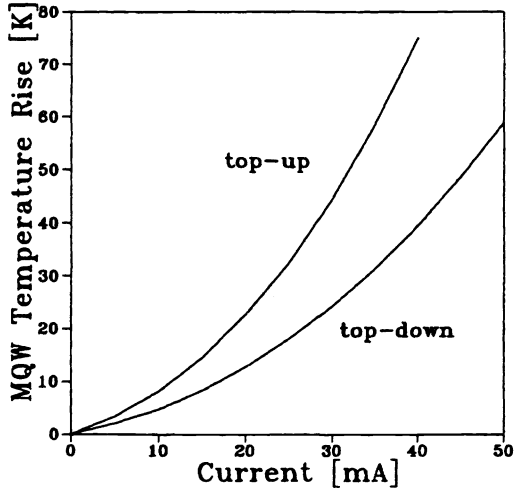


Figure 3: Average MQW temperature rise ΔT_a vs. current I with Si/SiO₂ top DBR and GaAs/AlAs bottom DBR in top-up and top-down mounting.

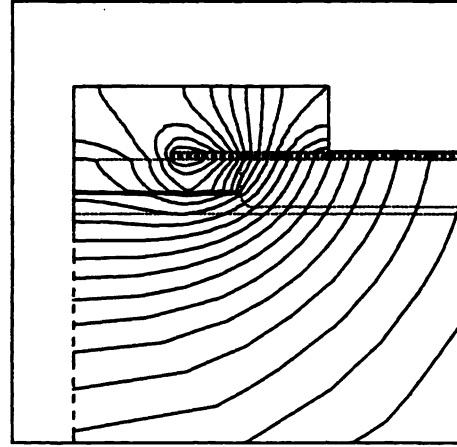


Figure 4: Contour plot of the temperature distribution $T(r, z)$ with Si/SiO₂ top DBR and GaAs/AlAs bottom DBR (top-up) at $I=50$ mA ($T_{max}=439$ K, $\Delta T=5$ K).

potential drop is quite small and diffusion is assumed to dominate the carrier transport. Holes, injected from the top, exhibit a much lower mobility than electrons, injected from the bottom, and electrons follow the hole distribution to recombine. The carrier density distribution $N(r)$ is calculated from the radial diffusion equation (7) with diffusion constant $D = 5 \text{ cm}^2\text{s}^{-1}$ and recombination rate R (see (15)). The influence of the optical field profile on $N(r)$ is not included in our model since effects like spatial hole burning¹⁰ are not of primary interest here. $N(r)$ near threshold is used (see Fig. 5) with $U_a=0.8$ V equal to the QW band gap voltage. Finally, nonuniform heat generation within the active region (total power $\approx U_a I$) and at the p-contact (total power $R_{con} I^2$) are identified as relevant heat sources in our device.

$$R - D \frac{1}{r} \frac{\partial}{\partial r} \left(r \frac{\partial N}{\partial r} \right) = \frac{1}{e d_a} j_a(r) \quad (7)$$

For the electro-thermal simulation, a multi-purpose 3D finite element code²⁴ is employed, permitting inhomogeneous, anisotropic, and temperature dependent material properties. This program obtains $j(r, z)$ (see Fig. 2) and $w_j(r, z)$ from (6). After adding the other heat sources, (1) is solved. In Fig. 3, the spatially averaged temperature rise within the active region ΔT_a is plotted against the current I . Top-down mounting clearly reduces the laser heating. At higher currents, contact heating dominates and the location of the maximum temperature T_{max} shifts from the MQW to the p-contact. A contour plot $T(r, z)$ is given in Fig. 4. The average temperature T_a of the active region and the temperature distribution $T(0, z)$ along the laser axis are applied in the following sections.

The thermal resistance R_{th} is often used for comparison of laser structures, obtained from the temperature rise and the total heat power P_a within the active region

$$R_{th} = \Delta T_a / P_a. \quad (8)$$

With low heating, this thermal parameter is almost independent on the current I as long as the active region is the only heat source, but it is found to depend on the heat power distribution *within* the active region. For comparison of top-down mounted LW-VCSELs with different DBR materials, R_{th} values are listed in Tab. 2 with low and uniform heating of the active region. The top DBR is covered with a highly reflective Au layer to lower

the number of top DBR sheets, keeping the amplitude reflectivity²⁵ near 99.98%. The bottom DBR material strongly influences the thermal resistance, i.e., heat flux spreading is essential not only in the InP regrowth region, but also in the DBR on the opposite side of the heat sink.¹⁷ The example in the first row of Tab. 2 is similar to the record-temperature LW-VCSEL in Ref.,² but it has the highest R_{th} value here because of the low thermal conductivity in the Si/SiO₂ bottom DBR. SiC/MgO or GaAs/AlAs top mirrors yield the lowest thermal resistances despite the higher number of layers. In these cases, R_{th} is almost independent on the mirror diameter since the average DBR thermal conductivity is similar to that of the In solder ($\kappa=0.87 \text{ Wcm}^{-1}\text{K}^{-1}$).

top DBR	bottom DBR	R_{th} [K/W]
3.5 × Si/MgO	4.5 × Si/SiO ₂	663
3.5 × Si/MgO	42.5 × InP/InGaAsP	562
3.5 × Si/MgO	28 × GaAs/AlAs	397
2.5 × Si/SiO ₂	28 × GaAs/AlAs	468
6.5 × SiC/MgO	28 × GaAs/AlAs	283
14 × GaAs/AlAs	28 × GaAs/AlAs	294

Table 2: Thermal resistances of LW-VCSELs mounted top-down with Au cover layer and In solder.

4 OPTICAL FIELD AT LASER THRESHOLD

The simulation procedure continues with the calculation of the optical field within the VCSEL at laser threshold. For VCSELs, the 3D waveguide equation is difficult to solve. In good approximation, we consider the vertical direction (z) only using the transfer matrix method.²⁶ Here, the propagation of forward and backward traveling waves through the layers is performed by matrix multiplications. The tangential field components must be continuous at the interfaces and, with a further inverse matrix multiplication, yield the wave amplitudes in the next layer.²⁷ Recursive calculations for all layers give the overall transfer matrix of this device. The laser condition (no incoming waves from outside) leads to an eigenvalue problem in the complex plane. From the real and imaginary parts of the eigenvalue, the emission wavelength λ_o and the threshold gain g_{th} can be found. The external quantum efficiency

$$\eta = |E_{out}|^2 / g_{th} d_a n_a |E_a|^2 \quad (9)$$

is then obtained from the intensity ratio $|E_{out}|^2/|E_a|^2$ of the emitted wave and the average optical field within the active region with n_a denoting the mean refractive index of the MQW. Heating is connected with a shift of the refractive index

$$n(T) = n(300\text{K}) + \beta \Delta T \quad (10)$$

with the sheet temperature rise $\Delta T = T - 300\text{K}$ obtained from the axial temperature profile $T(0, z)$ and with the material dependent coefficient β (see Tabs. 1 and 3). Using the value β of GaAs for all materials can cause substantial deviations in the final PI characteristic.¹² Optical absorption is mostly dominated by excitation of electrons within the conduction band or of holes within the valence bands and it is proportional to the carrier density N (see Tabs. 1 and 3). Especially in InGaAsP, strong intervalence band absorption (IVBA) emerges with high hole density and with long wavelengths, since the energy distance between the heavy hole band and the split-off band at higher wavevector values matches the photon energy. Compressive strain in QWs is observed to reduce IVBA compared to unstrained MQWs.^{28,29} With an average threshold hole density of $4 \cdot 10^{18} \text{ cm}^{-3}$, we use an IVBA coefficient within the quantum wells of 80 cm^{-1} at room temperature. Its temperature dependence due to the availability of heavy holes can be described by

$$\alpha_{IVBA}(T) = \alpha_{IVBA}(300\text{K}) \exp[\Delta T/T_o]. \quad (11)$$

with $T_o=34 \text{ K}$ (obtained from the heavy hole branch of Fig. 3 in Ref.³⁰). Additionally, we include thermal sheet expansion with the linear expansion coefficient $6 \cdot 10^{-6} \text{ K}^{-1}$, i.e., a 100 K temperature rise expands the layers by only 0.06%. Resulting optical parameters are plotted in Fig. 6 as function of the temperature T_a . Despite the

thermal improvement of the mirror reflectivities,¹² to be seen in the reduction of η , the threshold gain is strongly increased with temperature due to enhanced QW absorption. The wavelength shift rate $d\lambda_o/dT = 1.3 \text{ \AA}/\text{K}$ is in good agreement with measurements.²² Room temperature results for different devices are listed in Tab. 4. Here, top-down mounting with Au cover layer lowers g_{th} and heightens η compared to top-up mounting.

The threshold gain g_{th} is a radially averaged value. The carrier density N changes in radial direction and so does the optical gain $g(\lambda_o, N, T_a)$ obtained in the next section. At threshold, g_{th} is equal to the modal gain calculated from the overlap integral

$$\gamma = \frac{A_a}{2\pi} \int \Phi^2(r)g(r)r dr \times \left(\int \Phi^2(r)r dr \times \int g(r)r dr \right)^{-1} \quad (12)$$

of fundamental mode optical intensity $\Phi^2(r)$ and gain profile $g(r)$ within the active region. Thus, the radial optical field profile $\Phi(r)$ needs to be known. The boundary condition of the spatial waveguide problem requires, that the optical field vanishes at the Au p-contact and that its derivative is zero at the interface to the top DBR (lower refractive index). We assume that, also in the active layer, the optical field vanishes outside the top window radius of $3 \mu\text{m}$. The solution $\Phi(r)$ of this problem is approximated by the zero order Bessel function (see Fig. 5). The use of the radial temperature distribution is not yet included in our optical model. However, our device example is index guided and thermal lensing is assumed insignificant.

material	p-InP	InGaAsP	InGaAsP	n-InP
layer	top spacer	barrier	quantum well	bottom spacer
n at T=300K	3.17	3.4	3.6	3.17
$\beta=dn/dT [10^{-4} \text{ K}^{-1}]$	3	5	5	3
$\alpha [1/\text{cm}]$	24	0	80 ($T_o=34\text{K}$)	1

Table 3: Optical material parameters used in the calculations.

5 GAIN FUNCTION AND THRESHOLD CURRENT

The optical gain in the quantum wells is calculated in two steps.³¹ First, the band structure is determined taking into account valence-band mixing and the modification due to strain.³² The conduction subbands are assumed to have parabolic dispersion. The conduction band edge is modified only by the hydrostatic component of the strain and it is calculated by adopting the model of Ref.³³ The valence subbands are obtained using a 4×4 Luttinger-Kohn Hamiltonian in the axial approximation and neglecting terms linear to the wavevector. Both the hydrostatic and the shear component of the strain change the valence band structure. Having determined the band structure, the dipole matrix elements of all transitions between the conduction and valence subbands are calculated. It is assumed that the band structure as well as the dipole matrix elements do not depend on carrier density and temperature. In the second step, the optical gain as function of wavelength, carrier density and temperature is obtained. Thereby, we calculate first the spontaneous emission spectrum r_{sp} using the stored band structure, dipole matrix elements, and a Lorentzian broadening with a constant intra-band relaxation time. Then, the optical gain is determined via the relation

$$g(\omega, N, T) \propto \left[1 - \exp \left(\frac{\hbar\omega - eU_F(N, T)}{kT} \right) \right] r_{sp}(\omega, N, T) \quad (13)$$

where eU_F is the separation between the quasi-Fermi energies of holes and electrons and $\hbar\omega = hc_o/\lambda_o$ is the photon energy (h - Planck's constant, c_o - light velocity, k - Boltzmann constant). In this way, the transition from gain to absorption occurs at $\hbar\omega = eU_F$ as it should be and the unphysical situation that the gain changes its sign below the band gap is avoided. The net band gap $E_g(N, T)$ takes into account the carrier-density induced bandgap shrinkage due to exchange and correlation effects and the change of the bandgap due to the temperature

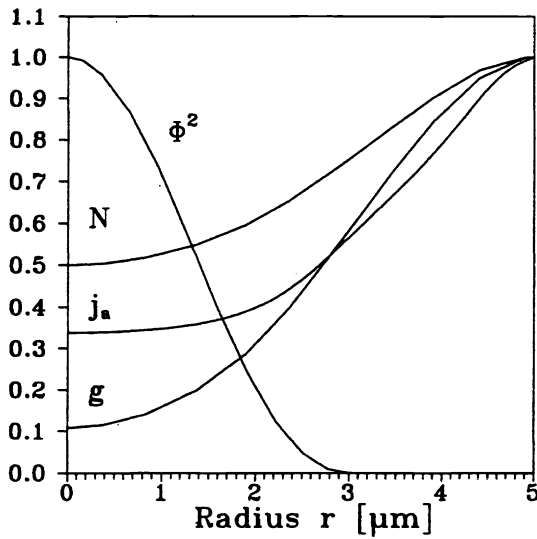


Figure 5: Normalized radial distribution of optical intensity Φ^2 , carrier density N , injection current density j_a , and gain g of the active region ($T=300\text{K}$).

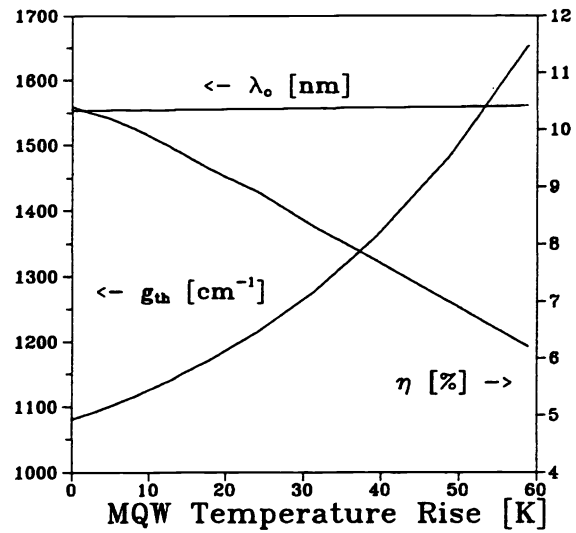


Figure 6: Threshold gain g_{th} , wavelength λ_o , and external efficiency η vs. temperature ΔT_a (top-down mounting, Si/SiO₂ top DBR, GaAs/AlAs bottom DBR).

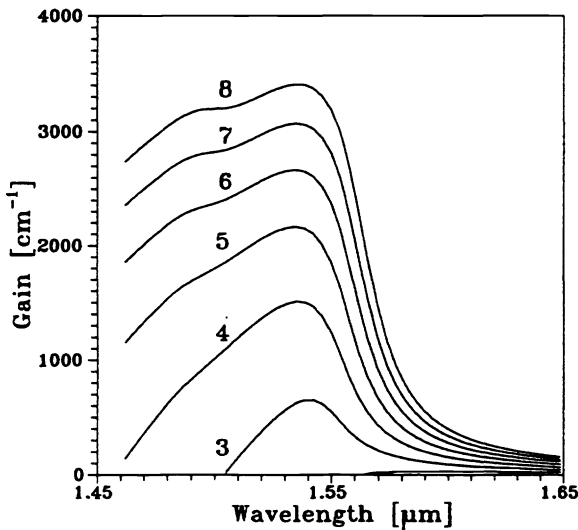


Figure 7: Optical gain of the strained MQW active region as function of the wavelength with the carrier density as parameter [10^{18}cm^{-3}] ($T_a=300 \text{K}$).

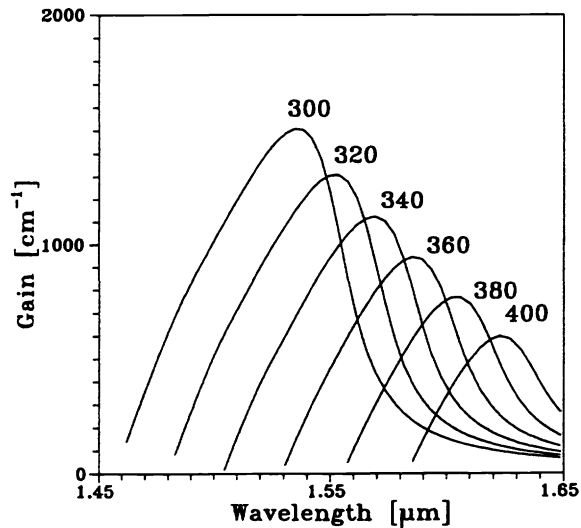


Figure 8: Optical gain of the MQW active region as function of the wavelength at different temperatures ΔT_a [K] ($N=4 \cdot 10^{18} \text{cm}^{-3}$).

dependent lattice constant and lattice vibrations ($dE_g/dT = -4 \cdot 10^{-4}$ eV/K). Figs. 7 and 8 show the calculated gain as function of wavelength, carrier density and temperature. The strain-compensated MQW is designed to exhibit the room temperature gain peak at $1.54 \mu\text{m}$ wavelength. The red-shift of the gain peak wavelength with temperature (Fig. 8) is stronger than the red-shift of the cavity wavelength λ_o (Fig. 6) and both wavelengths coincide somewhat above room temperature.

Using the gain function $g(\lambda_o, N, T_a)$, the average threshold carrier density N_{th} is obtained from the threshold condition

$$g_{th} = \gamma g(\lambda_o, N_{th}, T_a) \quad (14)$$

with the overlap integral $\gamma = 0.41$ calculated from the room temperature profiles given in Fig. 5. The threshold current

$$I_{th} = e d_a A_a (AN_{th} + BN_{th}^2 + CN_{th}^3) \quad (15)$$

includes the rate R of Shockley-Read-Hall (SRH) recombination, spontaneous emission, and Auger recombination ($A = 2 \cdot 10^8 \text{ s}^{-1}$, $B = 10^{-10} \text{ cm}^3\text{s}^{-1}$, $C = 10^{-28} \text{ cm}^6\text{s}^{-1}$). The Auger coefficient C is hardly affected by strain and only weakly dependent on temperature³⁴ ($T_o=100$ K). The different contributions to the threshold current density $j_{th} = I_{th}/A_a$ are shown in Fig. 9 as function of the temperature T_a . In this example, the gain peak shift leads to a j_{th} minimum at $T_a \approx 310$ K with a minimum N_{th} of $3.8 \cdot 10^{18} \text{ cm}^{-3}$. Initiated by the thermal increase of g_{th} and N_{th} , Auger recombination seems to be the strongest mechanism to raise I_{th} with increased temperature and to finally cause the roll-over of the PI curve. Leakage current due to recombination outside the QWs is negligible because of the small total barrier thickness and the absence of electrical confinement layers in our device (see Ref.¹⁰). Tab. 4 gives a summary of calculated LW-VCSEL parameters at room temperature. I_{th} and j_{th} values listed are close to results measured on similar devices in pulsed operation,⁵⁻⁸ where heating effects are negligible.

top DBR	bottom DBR	mounting	g_{th}/γ	η	N_{th}	I_{th}	j_{th}
			1/cm	%	$1/\text{cm}^3$	mA	kA/cm^2
$5 \times \text{Si}/\text{SiO}_2$	$42.5 \times \text{InP}/\text{InGaAsP}$	top-up	1373	3.1	$4.6 \cdot 10^{18}$	8.2	10.4
$5 \times \text{Si}/\text{SiO}_2$	$28 \times \text{GaAs}/\text{AlAs}$	top-up	1124	3.8	$4.5 \cdot 10^{18}$	8.0	10.2
$2.5 \times \text{Si}/\text{SiO}_2$	$28 \times \text{GaAs}/\text{AlAs}$	top-down	1080	10.4	$4.0 \cdot 10^{18}$	5.9	7.5
$6.5 \times \text{SiC}/\text{MgO}$	$28 \times \text{GaAs}/\text{AlAs}$	top-down	1067	10.6	$4.0 \cdot 10^{18}$	5.7	7.3
$14 \times \text{GaAs}/\text{AlAs}$	$28 \times \text{GaAs}/\text{AlAs}$	top-down	1124	10.3	$4.0 \cdot 10^{18}$	5.6	7.1
$3.5 \times \text{Si}/\text{MgO}$	$28 \times \text{GaAs}/\text{AlAs}$	top-down	1076	10.5	$4.0 \cdot 10^{18}$	5.8	7.4
$3.5 \times \text{Si}/\text{MgO}$	$4.5 \times \text{Si}/\text{SiO}_2$	top-down	1027	19.9	$4.2 \cdot 10^{18}$	6.5	8.3

Table 4: Calculated parameters of LW-VCSELs at $T=300$ K ($\lambda_o \approx 1553$ nm).

6 LIGHT POWER

The temperature dependent device parameters η , λ_o , and I_{th} change with rising current I and affect the emitted light power

$$P(I) = h c_o \eta (I - I_{th}) / e \lambda_o. \quad (16)$$

The influence of the heat source distribution on the resulting PI curves is shown in Fig. 10. Contact heating strongly reduces the maximum light power P_{max} but the nonuniform MQW heat generation lowers T_a relative to a uniform heat source. Different DBR combinations are compared in Figs. 11 and 12. The top-up mounted devices show the lowest P_{max} values, caused by stronger heating, but also by smaller external efficiency than with top-down mounting (see Tab. 4). In top-down mounting, SiC/MgO and GaAs/AlAs top DBRs lead to higher P_{max} values at higher currents than the Si/MgO combination from Ref.² The device with SiC/MgO top DBR in Fig. 12 exhibits a higher P_{max} than with Si/SiO₂ mirror despite nearly identical room temperature parameters in Tab. 4. Thus, the different thermal resistances (see Tab. 2) are of major influence in this case.

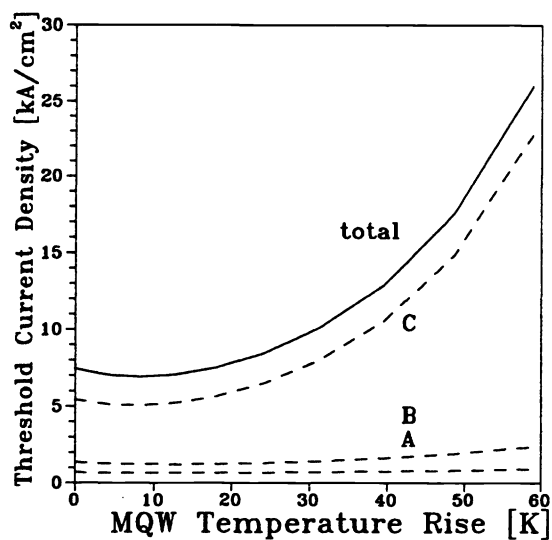


Figure 9: Contributions to $j_{th}(\Delta T_a)$ from SRH recombination (A), spontaneous emission (B), and Auger recombination (C) (top-down mounting, Si/SiO₂ top DBR, GaAs/AlAs bottom DBR).

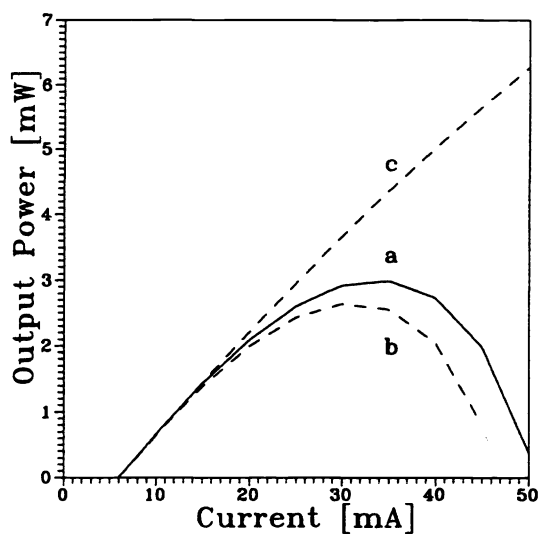


Figure 10: *PI* characteristics with Si/MgO top DBR and Si/SiO₂ bottom DBR (top-down) with all heat sources (a), homogeneous active region heat generation (b), and without contact heating (c).

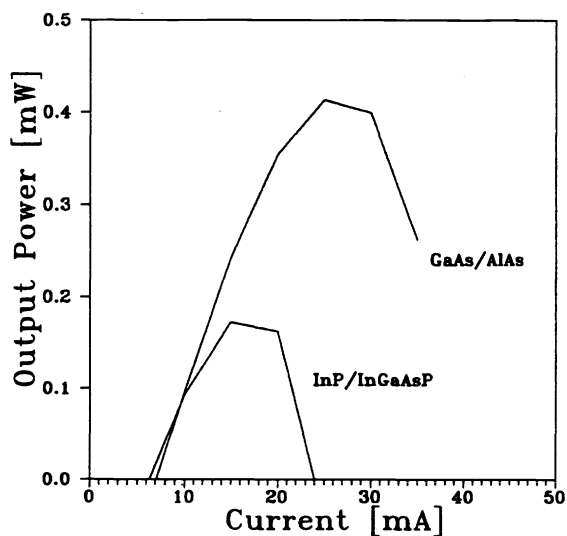


Figure 11: *PI* characteristics with different bottom DBRs and Si/SiO₂ top DBR mounted top-up.

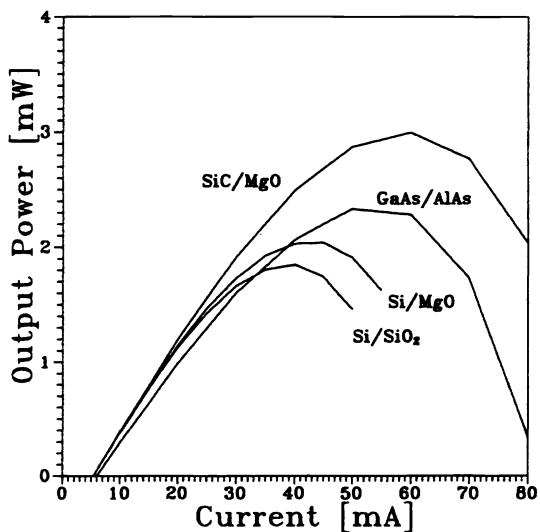


Figure 12: *PI* characteristics with different top DBRs and GaAs/AlAs bottom DBR mounted top-down.

But, comparing curve (a) in Fig. 10 and the SiC/MgO curve in Fig. 12, the P_{max} values are almost identical despite strong differences in R_{th} . The smaller thermal resistance of the SiC/MgO device is compensated here by the lower external quantum efficiency (see Tab. 4). Practically, the top-down mounted devices with SiC/MgO or GaAs/AlAs top mirror and GaAs/AlAs bottom mirror are assumed to give the best results because of small thermal resistance and low mirror absorption compared to Si DBRs.

Measurements on real LW-VCSELs are not available to fit these simulated results. Material parameters like absorption coefficients and their temperature dependence need to be determined. However, this theoretical comparison of different DBR materials for LW-VCSELs is expected to be instructive for further device development.

7 REFERENCES

- [1] K. Iga and S. Uchiyama, "GaInAsP/InP surface-emitting laser diode," *Opt. Quant. Electr.*, Vol. 18, pp. 403-422, 1986.
- [2] T. Baba, Y. Yogo, K. Suzuki, F. Koyama, and K. Iga, "Near room temperature continuous wave lasing characteristics of GaInAsP/InP surface emitting lasers," *Electronics Letters*, Vol. 29, pp. 913-914, 1993.
- [3] M. A. Fisher, A. J. Dann, D. A. O. Davies, D. J. Elton, M. J. Harlow, C. B. Hatch, S. D. Perrin, J. Reed, I. Reid, and M. J. Adams, "High temperature photopumping of 1.55 μ m vertical cavity surface emitting lasers," *Electronics Letters*, Vol. 29, pp. 1548-1550, 1993.
- [4] D. I. Babic, J. J. Dudley, K. Streubel, R. P. Mirin, E. L. Hu, and J. E. Bowers, "Optically pumped 1.52- μ m vertical-cavity lasers," *El. Lett.*, Vol. 30, pp. 704-705, 1994.
- [5] J. J. Dudley, D. I. Babic, R. Mirin, L. Yang, B. I. Miller, R. J. Ram, T. Reynolds, E. L. Hu, and J. E. Bowers, "Low threshold, wafer fused long wavelength vertical cavity lasers," *Appl. Phys. Lett.*, Vol. 64, pp. 1463-1465, 1994.
- [6] D. I. Babic, J. J. Dudley, K. Streubel, R. P. Mirin, N. M. Margalit, J. E. Bowers, and E. L. Hu, "Double-fused 1.52- μ m vertical-cavity lasers," *IEEE/LEOS Annual Meeting*, paper PD1.4, Boston, 1994.
- [7] K. Uomi, S. J. B. Yoo, A. Scherer, R. Bhat, N. C. Andeadakis, C. E. Zah, M. A. Koza, and T. P. Lee, "Low threshold, room temperature pulsed operation of 1.5 μ m vertical-cavity surface-emitting lasers with an optimized multi-quantum well active layer," *IEEE Phot. Techn. Lett.*, Vol. 6, pp. 317-319, 1994.
- [8] H. Wada, D. I. Babic, M. Ishikawa, and J. E. Bowers, "Effect of nonuniform current injection in GaInAsP/InP vertical-cavity lasers," *Appl. Phys. Lett.*, Vol. 60, pp. 2974-2976, 1992.
- [9] C. H. Lin, C. L. Chua, Z. H. Zhu, F. E. Ejeckam, T. C. Wu, and Y. H. Yo, "Photopumped long wavelength vertical-cavity surface-emitting lasers using strain-compensated multiple quantum wells," *Appl. Phys. Lett.*, Vol. 64, pp. 3395-3397, 1994.
- [10] J. W. Scott, R. S. Geels, S. W. Corzine, and L. A. Coldren, "Modeling Temperature Effects and Spatial Hole Burning to Optimize Vertical-Cavity Surface-Emitting Laser Performance," *IEEE J. Quant. El.*, Vol. 29, pp. 1295-1308, 1993.
- [11] R. Michalzik and K. J. Ebeling, "Modeling and Design of Proton-Implanted Ultralow-Threshold Vertical Cavity Laser Diodes," *IEEE J. Quant. El.*, Vol. 29, pp. 1963-1974, 1993.
- [12] J. Piprek, H. Wenzel, and G. Sztafka, "Modeling thermal effects on the light vs. current characteristic of gain-guided vertical-cavity surface-emitting lasers," *IEEE Phot. Techn. Lett.*, Vol. 6, pp. 139-142, 1994.
- [13] L. E. Thode, G. Csanak, L. L. So, and T. J. T. Kwan, "Time-dependent numerical simulation of vertical cavity laser," *SPIE Proc.*, Vol. 2146, pp. 174-184, 1994.

- [14] M. Shimizu, D. I. Babic, J. J. Dudley, W. B. Jiang, and J. E. Bowers, "Thermal resistance of $1.3\mu\text{m}$ InGaAsP vertical cavity lasers," *Microw. Opt. Techn. Lett.*, Vol. 6, pp. 455-457, 1993.
- [15] M. Osinski and W. Nakwaski, "Effective thermal conductivity analysis of $1.55\mu\text{m}$ InGaAsP/InP vertical-cavity top-surface-emitting microlasers," *Electronics Letters*, Vol. 29, pp. 1015-1016, 1993.
- [16] J. Piprek and S. J. B. Yoo, "Thermal comparison of long-wavelength vertical-cavity surface-emitting laser diodes," *El. Lett.*, Vol. 30, pp. 866-868, 1994.
- [17] J. Piprek, "Heat flow analysis of long-wavelength VCSELs with various DBR materials," *IEEE/LEOS Annual Meeting*, Proc. pp. 286-287, Boston, 1994.
- [18] D. G. Deppe, D. L. Huffaker, C. C. Lin, and T. J. Rogers, "Nearly planar low threshold vertical-cavity surface-emitting lasers using high contrast mirrors and native oxidation," *Conf. on Lasers and Electro-Optics CLEO*, CPD2, Anaheim, 1994.
- [19] D. I. Babic, Y. Chung, N. Dagli, and J. E. Bowers, "Modal reflection of quarter-wave mirrors in vertical-cavity lasers," *IEEE J. Quant. Electr.*, Vol. 29, pp. 1950-1962, 1993.
- [20] G. P. Agrawal and N. K. Dutta, *Semiconductor Lasers*, Van Nostrand Reinhold, New York, 1993.
- [21] S. Adachi, *Physical Properties of III-V Semiconductor Compounds*, John Wiley & Sons, New York, 1992.
- [22] J. J. Dudley, "Wafer Fused Vertical Cavity Lasers," Ph.D. Thesis, University of California, Santa Barbara, 1994.
- [23] OPTIMATR Version 2.11 (1993) by ARSoftware, Landover, MD, USA.
- [24] ANSYS Revision 5.0 (1993) by Swanson Analysis, Houston, PA, USA.
- [25] S. W. Corzine, R. H. Yan, and L. A. Coldren, "A tanh substitution technique for the analysis of abrupt and graded interface multilayer dielectric stacks," *Quant. Electron. Lett.*, Vol. 27, pp. 2086-2090, 1991.
- [26] Program written by G. Sztefka, improved by J. Piprek and H. Wenzel.
- [27] J. Chilwell and I. Hodgkinson, "Thin-film field-transfer matrix theory of planar multilayer waveguides and reflection from prism-loaded waveguides," *J. Opt. Soc. Am. A*, Vol. 1, pp. 742-753, 1984.
- [28] G. Fuchs, "Verlustprozesse und optische Verstärkung in InGaAs-Quantenfilmlasern," Dissertation, Universität Stuttgart, Stuttgart, 1993.
- [29] I. Joindot and J. L. Beylat, "Intervalence band absorption coefficient measurements in bulk layer, strained and unstrained multiquantum well $1.55\mu\text{m}$ semiconductor lasers," *Electron. Lett.*, Vol. 29, pp. 604-606, 1993.
- [30] A. R. Adams, M. Asada, Y. Suematsu, and S. Arai, "The temperature dependence of the efficiency and threshold current of $\text{In}_{1-x}\text{Ga}_x\text{As}_y\text{P}_{1-y}$ lasers related to intervalence band absorption," *Jap. J. Appl. Phys.*, Vol. 10, pp. L621-L624, 1980.
- [31] Program written by M. Willatzen, improved by M. Ritze and H. Wenzel.
- [32] M. Willatzen, "Theory of gain in bulk and quantum-well semiconductor lasers," Ph.D. Thesis, University of Copenhagen and TFL Hørsholm, Copenhagen, 1993.
- [33] C.G. Van de Walle, "Band lineups and deformation potentials in the model-solid theory," *Phys. Rev. B*, Vol. 39, pp. 1871-1883, 1989.
- [34] G. Fuchs, C. Schiedel, A. Hangleiter, V. Härle, and F. Scholz, "Auger recombination in strained and unstrained InGaAs/InGaAsP quantum well lasers," *J. Appl. Phys.*, Vol. 62, pp. 396-398, 1993.